Nanoscale

Full paper

Cite this: DOI: 10.1039/xxxxxxxxxx

Optical Properties of GaN/AlN Quantum-Wires Grown on Nanowire Templates

Jan Müßener[1,2*], Ludwig A. Th. Greif[3*], Stefan Kalinowski[3], Gordon Callsen[3], Pascal Hille[1,2], Jörg Schörmann[2], Markus R. Wagner[3], Andrei Schliwa[3], Sara Martí-Sánchez[4], Jordi Arbiol[4,5], Axel Hoffmann[3], Martin Eickhoff[1,2]

Received Date
Accepted Date

DOI: 10.1039/xxxxxxxxxx

www.rsc.org/journalname

We show that one-dimensional (1d) GaN quantum wires (QWRs) exhibit intense and spectrally sharp emission lines. These QWRs are realized in an entirely self-assembled growth process by molecular beam epitaxy (MBE) on the side facets of GaN/AlN nanowire (NW) heterostructures. Time-integrated and time-resolved photoluminescence (PL) data in combination with numerical calculations allow the identification and assignment of the manifold emission features to three different spatial recombination centers within the NW. The recombination processes in the QWRs driven by efficient charge carrier transfer effects between the different optically active regions, providing high intense QWR luminescence despite their small volume. This is deduced by a fast rise time of the QWR PL, which is similar to the fast decay-time of adjacent carrier reservoirs. Such processes, feeding the ultra-narrow QWRs with carriers from the relatively large NW, can be the key feature towards realization of future QWR-based devices. While processing of single quantum structures with diameters in the nm range presents a serious obstacle with respect to their integration into electronic or photonic devices, the QWRs presented here can be analyzed and processed using existing techniques developed for single NWs.

0.1 Introduction

Since the first pioneering works on semiconductor superlattice structures[1–4] and reports about specific characteristics, such as an improved carrier mobility[5] the reduction of dimensionality has opened new research fields and applications in semiconductor physics.

The influence of quantum confinement on the density of states[6] as well as reduced scattering of electrons[7] moved low dimensional semiconductors into the focus of optical applications, such as lasers and amplifiers.[6,8,9] Within the variety of structures with different dimensionality, quasi one-dimensional objects with diameters below the exciton-Bohr radius, also known as QWR, stand out due to their potential to outperform 2d heterostructures with respect to their high mobility in combination with higher temperature stability and narrower spectral line width.[6,7,10]

While first attempts to realize QWRs were focused on Si[11,12] and AlGaAs[13], their synthesis has later been reported for other material systems including GaN with its superior optical properties as direct wide band-gap material[14–20]. Recently, owing to the progress in the manufacturing of various material systems, QWRs also became attractive structures for photonic devices as LEDs[21], solar cells[22] and photo cathodes.[23]. So far, all reported realizations of wires with diameters below 10 nm use one of the following fabrication techniques: i) chemical etching[24], ii) vapor-liquid-solid (VLS) growth[14,15,17], iii) catalytic growth assisted by transition metals[18] or iv) template induced growth by carbon nanotube replacement.[19]

All these techniques lack the potential to grow QWR of small diameters with predefined positions and orientation. And although electrical contacts were already realized for NWs with diameters lager than 80 nm[25], direct contacting of much smaller QWRs is difficult to achieve. Thus, significant hurdles exist with respect to their integration into devices. To overcome these obstacles, we build our work on QWRs, produced by an innovative self-assembled template-induced approach[26], basically enabling the realization of position-controlled QWRs by combination with site selective bottom-up[27,28] or top-down[29] NW growth techniques.

In this letter, we present a detailed study of the optical properties of single GaN QWRs, using time-integrated and time resolved micro photoluminescence spectroscopy (TR-μPL). The experimental results are complemented by 8-band **kp** simulations

[1] *Institut für Festkörperphysik, Universität Bremen, Germany*
[2] *I Physikalisches Institut, Justus-Liebig-Universität Gießen, Germany*
[3] *Institut für Festkörperphysik, Technische Universität Berlin, Germany*
[4] *Catalan Institute of Nanoscience and Nanotechnology (ICN2), CSIC and BIST, Campus UAB, Bellaterra, 08193 Barcelona, Catalonia, Spain*
[5] *ICREA, Pg. Lluis Companys 23, 08010 Barcelona, Catalonia, Spain*
[*] Authors contributed equally and share first authorship

considering strain, piezoelectric and pyroelectric effects. Thus, we can establish a direct correlation between different spectral features and their spatial origin on a sub 30 nm scale. Furthermore, we present clear indications for charge transfer processes between three spatially separated carrier reservoirs in the NW heterostructure.

The manuscript is organized as follows. After the description of the sample structure, the applied experimental and simulation methods, we present a μ-PL analysis that reveals different emission features with specific intensity, linewidth and power-dependence. By comparison with simulations of transition energies and lifetimes, considering different geometries and carrier concentrations, the features are assigned to spatially separated emission centers. Next, the decay dynamics are investigated by TR-μPL spectra and corresponding simulations, providing insight in a carrier transfer process between different parts of the NW including the QWRs. In a final discussion, the mutual interaction of local carrier concentration and carrier dynamics is discussed and a term scheme for the involved transitions and transfer processes is developed.

0.2 Methods

GaN/AlN NW samples were grown catalyst-free by plasma-assisted molecular beam epitaxy (PAMBE) on Si(111) substrates in wurtzite structure along the polar [000$\bar{1}$] direction (N-face polarity) using nitrogen-rich conditions.[26] Fig. 1 a shows a scanning transmission electron microscope (STEM) image of the heterostructure in high angle annular dark-field (HAADF) contrast with GaN appearing in brighter and AlN in darker contrast. Primarily, GaN NWs (core) with a length of 500 nm and a diameter of 25 nm serve as templates for an AlN/GaN/AlN heterostructure overgrowth. Growth of the lower AlN barrier exhibits deviations from the strict hexagonal facetted shape, with exposed {11$\bar{2}$0} facets (a-plane) at the six edges. The subsequent growth of GaN forms lateral QWRs along these edges (cf. 1 d) and an axial disc with a height of 28 nm, i.e. too large to exhibit geometric confinement. Due to shadowing effects the lateral overgrowth is limited to the upper $\approx$ 100 nm part of the existing NW below. The substrate temperature during growth was 720 °C and the beam equivalent pressure of the Ga or Al effusion cells was $2.6 \cdot 10^{-7}$ mbar for the lower GaN core, $5.1 \cdot 10^{-7}$ mbar for the middle GaN disc/QWR and $7.7 \cdot 10^{-8}$ mbar for the AlN barriers. Nitrogen was provided during growth by a radio frequency plasma source. Further details of the growth process can be found in ref. 26.

In order to allow μPL analysis of single NWs, the wires were removed from the substrate by ultrasonication in isopropanol and dispersed on a SiO_2 substrate, featuring marker structures for SEM correlation. The measurements were performed using a frequency-quadrupled Nd:YAG Laser at 266 nm with 76 MHz repetition rate and 5.5 ps pulse duration. The laser spot was focused on the sample using a 20x UV-objective with NA 0.4 mounted on a piezo-positioner. Samples were mounted in a continuous-flow cryostat at a temperature of 8 K. For time-integrated spectra a grating monochromator with 1200 lines/mm grating and a liquid

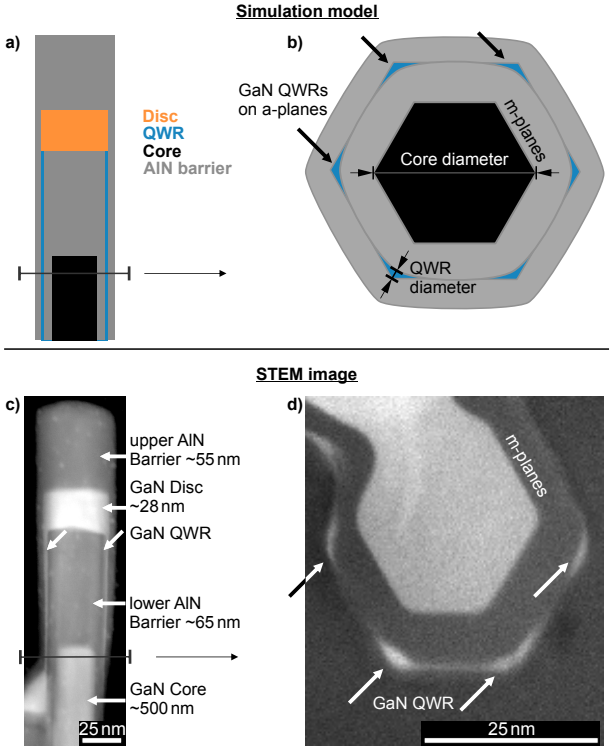

Fig. 1 (a) Scheme of the heterostructure for the numerical model and cross section (b) with embedded QWRs at the a-planes of the AlN intersection. (c) STEM (HAADF) microscopy of the GaN/AlN NW heterostructure on top of a single GaN NW plus cross section (d). The GaN QWRs (bright contrast) are visible laterally on the lower AlN barrier.

nitrogen cooled CCD were used. Time-resolved transients were recorded using a photomultiplier detector in single photon counting mode with a temporal resolution of $<$10 ps (Picoquant PMA hybrid) attached to a double monochromator with a focal length of 0.35 m.

For structural characterization by STEM, single NWs were prepared by mechanical scratching from the underlying template. Subsequently, the NWs were dispersed on an electron-transparent carbon-membrane TEM-grid. The measurements were performed using a FEI STEM Tecnai F20. Here, the forward scattered electrons are detected by a high angle annular dark field detector (HAADF) from Fischione (model 3000). The STEM acceleration voltage was set to 200 kV to analyses the NW microstructure.

In addition, in order to characterize the NW cross-section, we prepared Focus Ion Beam (FIB) cuts by using a FEI Helios 600 Dual Beam microscope, which provided thin (50-100 nm) lamellae across the nanowire. The cross-sections were later inspected by high angle annular dark-field scanning transmission electron microscopy (HAADF-STEM) using a probe corrected FEI Titan 60-300 equipped with a high brightness field emission gun (XFEG) and a CETCOR corrector from CEOS.

The geometry information from STEM investigations (Fig. 1 a,b) was implemented for computational modeling of the upper part of the NW which contains the actual heterostructure (Fig. 1 c,d).

Calculations of the band structure as well as investigations of

the size-dependent transition characteristics are performed using eight-band **kp**-theory including effects of strain, piezo-, and pyroelectricity.[30,31] Thereby, the strain distribution is calculated employing a continuum mechanical model.[32] The results are found to be highly sensitive to internal electric fields and thus, to possible screening effects by photogenerated free carriers or residual doping.

The effect of mutual carrier screening is considered by including more than 1000 electron-hole-pairs, corresponding to carrier densities in the $10^{19}\,\mathrm{cm}^{-3}$ range. To reduce the computational costs, a Hartree-inspired method is employed, which includes only the direct part of the Coulomb interaction. The solution for the n-th electron is then obtained by adding the Coulomb potential of the n-1 electrons, C_e, and n holes, C_h, to the single-particle **kp** Hamiltonian, H_{kp}, and thus creating the effective Hamiltonian, $H_{n,e}$ and $H_{n,h}$, for the n-th electron and hole states, respectively:

$$H_{n,e} = H_{kp} + \sum_{i=1}^{n-1} C_{i,e} + \sum_{i=1}^{n} C_{i,h} \tag{1}$$

$$H_{n,h} = H_{kp} + \sum_{i=1}^{n} C_{i,e} + \sum_{i=1}^{n-1} C_{i,h} \tag{2}$$

Due to the large number of interacting particles the solution of this effective Hamiltonian is obtained without self-consistency to the assigned Coulomb potentials $C_{e,h}$. Thus, the repercussion of the n-th electron onto all n-1 electrons and n holes is neglected. Although this simplification may lead to inhomogeneous charge distributions for a certain number of electrons and holes, it converges towards a homogeneous distribution with increasing carrier concentration.

0.3 Results

Time-integrated and power-dependent μPL emission spectra of single NWs, which may contain up to six QWRs, are shown in Fig. 2. Here, NWs from two different samples are probed, grown with a Ga beam equivalent pressure in the GaN disc/QWR region of $3.9{\cdot}10^{-7}$ mbar (sample A) and $5.1 \cdot 10^{-7}$ mbar (sample B), respectively. Both samples exhibit several emission bands that strongly differ in power dependence and linewidth. Anticipating the results of the simulations, they are labeled as core, disc and QWR emission. Disc and core emission are located at 3.3 – 3.5 eV and often overlap each other. The QWR emission is always found at higher energies in the range of 3.6 – 4.0 eV, sometimes up to 4.4 eV. While the core and QWR signals show no spectral shift for variations in excitation power, all disc signals have a pronounced power dependence.

To assign the spectral features to different locations within the complex NW heterostructure, simulations of the band profiles, transition energies and lifetimes were performed, illustrated in Fig. 3-5. The calculated internal electric field in the disc is in the order of several MV/cm while it almost vanishes within the QWRs and the main part of the core (Fig. 3 a,b). Calculated band profiles along the c-axis (Fig. 3 b,c) show relatively flat bands for the QWR, while the disc and upper core region in the vicinity of the interface to the AlN barrier exhibit pronounced polarization-induced internal electric fields. The resulting tilt in the conduction and valence band cause a significant reduction of the effective band gap for spatial indirect transitions in the disc region, and hence to a pronounced dependence of the transition energy on the screening of the internal fields. To probe this relation, and to explain the power dependent experimental data, simulations with successive screening of the interface charges due to increased carrier concentrations were performed.

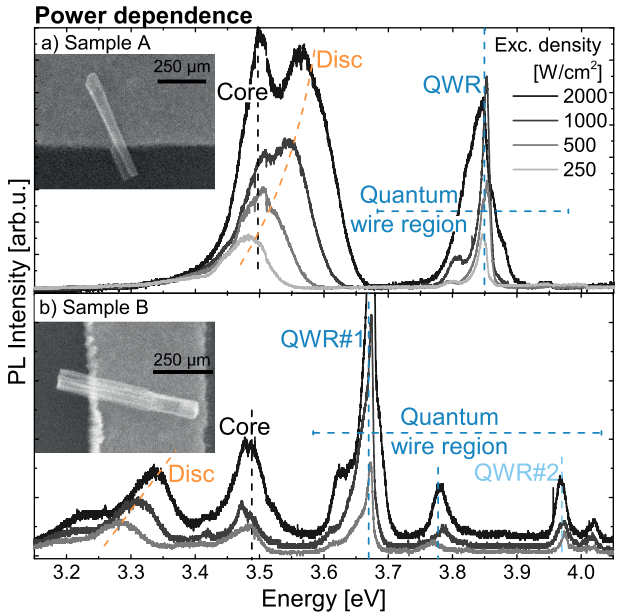

Fig. 2 (a, b) Power-dependent single-NW μPL spectra of sample A and B. The assignments of the spectral features to the core, the disc and the QWR are indicated. Insets show SEM images of the respective NW.

To consider different field strength, the Hartree-like method is used to calculate the transition energy and radiative lifetime as a function of the carrier concentration in the system (Fig. 4). Here, we show a strong blue shift and a decreasing decay time of the disc emission with increasing excitation power. Since the calculation scheme lacks exchange interaction, both, attractive and repulsive terms between charge carriers of same respective opposite charge are omitted. Considering low carrier concentrations with well separated electron-holes this means that mainly attractive parts are missing due to the insignificantly small electron-hole overlap. Consequently, the calculated lifetimes for low carrier concentrations are rather qualitatively than quantitatively. However, although band profiles of the core show a reduced effective bandgap, Hartree calculations reveal that only a few electron hole pairs are necessary to transform the interface charges at the core from unscreened to completely screened. Moreover, except for the simulated upper core part close to the interface, the main lower part is initially field-free. Thus, the transition energy and radiation lifetime of both the core and QWR exhibit almost no dependence on the concentration of free carriers.

To study and to separate the influence of geometry, completely screened internal electrical fields are considered, corresponding to highly photoexcited structures where a sufficiently high free carrier concentration compensates the polarization-induced inter-

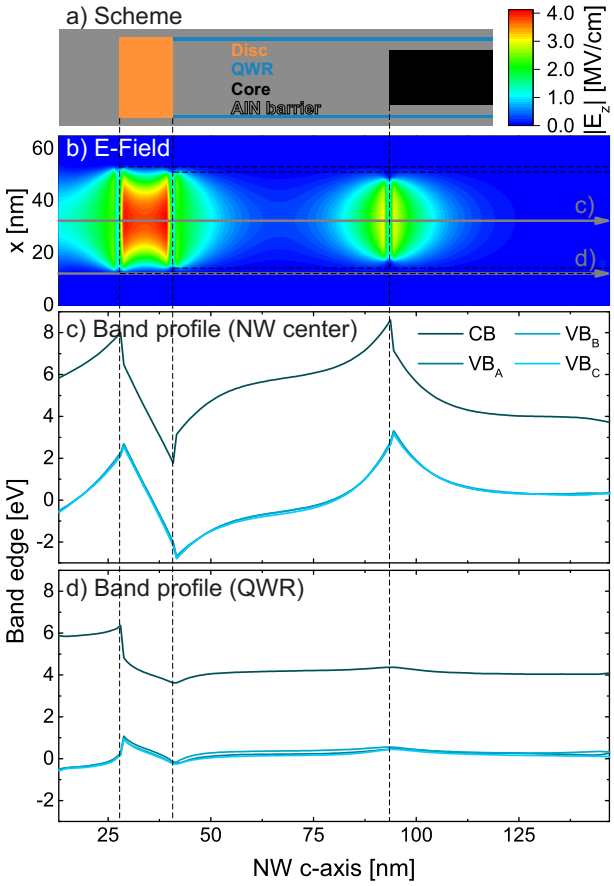

Fig. 3 (a) Scheme of the NW center plane. (b) Calculated absolute value of the z-component of the internal electric fields in the x-z-plane of a NW with: $d_{QWR} = 1.6$ nm; $d_{core} = 31.2$ nm; $h_{disc} = 15.2$ nm. Local CB-(black) and VB-edges (blue) shown along the c-axis through disc and core (c) and along a QWR (d).

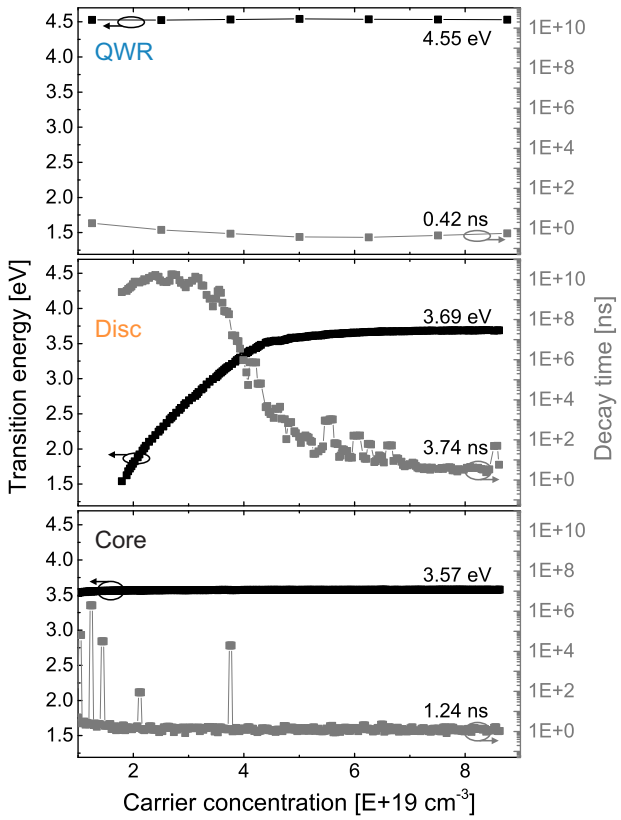

Fig. 4 Radiative lifetime (grey, right axis) and transition energy (black, left axis) as function of the carrier concentration, calculated with the Hartree-like method for the QWR (a), disc (b) and core (c). Outliers can be justified by the lack of a self-consistent charge distribution. Assumed sizes: $d_{QWR} = 1.6$ nm; $d_{core} = 31.2$ nm; $h_{disc} = 15.2$ nm.

face charges.

In this case, the variation of the core diameter, the disc height and the QWR diameter yields two energetically well separated spectral emission regimes (Fig. 5). In the lower energy range between 3.5 and 3.7 eV the spectrum is dominated by recombination inside the core (black) and the disc (orange), where the size dependence is introduced via the hydrostatic strain.[33] In contrast to the simulation model, all samples show a GaN core which lacks any AlN-shell in the lower part. Consequently, this strain-free bulk like GaN structure causes a near-band-edge (NBE) peak with no sample to sample variation in the experimental data. The wider emission range at higher energies originates from the QWRs (blue). Due to the radial confinement in the QWR the transition energy shows a strong dependence on the QWR diameter and spans a wide range from 3.9 up to 4.6 eV for diameters between 4 and 1.6 nm. This pronounced dependence of transition energies on diameter variation in the monolayer range[26] and the possible presence of multiple QWRs per NW, most probably gives rise to the observed manifold QWR signals.

Hence, based on the simulations three distinct features can be identified and assigned to different regions in the power-dependent spectra of Fig. 2. The emission band at 3.47 eV can be attributed to the NBE of the GaN core (Fig. 2, labelled core). Since no energy-shift is observed compared to homogeneous GaN NWs[34,35], this emission originates from the strain-free lower part of the NW where no AlN shell is present. As the emission energy does not vary with increasing excitation power no confinement potential or considerable internal electric fields has to be considered.

A second emission peak near the core NBE emission can be assigned to the GaN disc (Fig. 2, labelled disc). This emission is red shifted due to the quantum-confined Stark effect (QCSE) and thus shifts to higher energies with increasing excitation power owing to a partial compensation of the polarization-induced charges (Fig. 4 b) by photo-generated carriers.[36,37] Furthermore, the AlN barriers and the shell surrounding the GaN disc introduce compressive strain and cause a blue shift counteracting the redshift of the QCSE. Hence, the emission energy sensitively depends on the geometry of disc and barrier and varies slightly from wire to wire. Therefore, the disc emission can be found either at slightly higher energies than the NBE, as for sample A (Fig. 2 a), or slightly smaller, as for sample B (Fig. 2 b) and can even shift across the core emission when the excitation power is varied.

The emission in the range of 3.6 – 4.0 eV originates from the QWRs (Fig. 2, labelled QWR) and varies between different NWs in terms of intensity, energetic position and number of peaks, as

Table 1 Experimental rise and decay times of the samples A and B for disc, core and QWR in comparison to simulated optical decay times

sample	region	τ_{rise}	τ_{fast}	τ_{slow}	τ_{sim}
A	QWR	50 ± 2 ps	136 ± 0.7 ps	0.86 ± 0.05 ns	0.42 ns
	core	—	< 30 ps	1.79 ± 0.09 ns	1.24 ns
	disc	—	< 30 ps	8.8 ± 0.2 ns	3.74 ns*
B	QWR#1; 2	< 30 ps; < 30 ps	144 ± 3 ps; 108 ± 4 ps	1.19 ± 0.06 ns; 1.9 ± 0.2 ns	0.42 ns
	core	—	< 30 ps	1.03 ± 0.08 ns	1.24 ns
	disc	—	190 ± 60 ps	3.5 ± 0.6 ns	3.74 ns*

* saturation value for high carrier concentrations (cf. Fig. 6b)

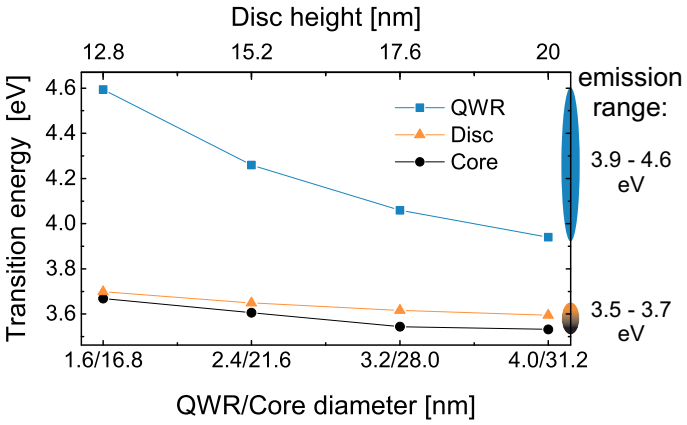

Fig. 5 Transition energy for single particle ground states located in the QWR (blue), the disc (orange) and the core (black) for different sizes with completely screened internal fields.

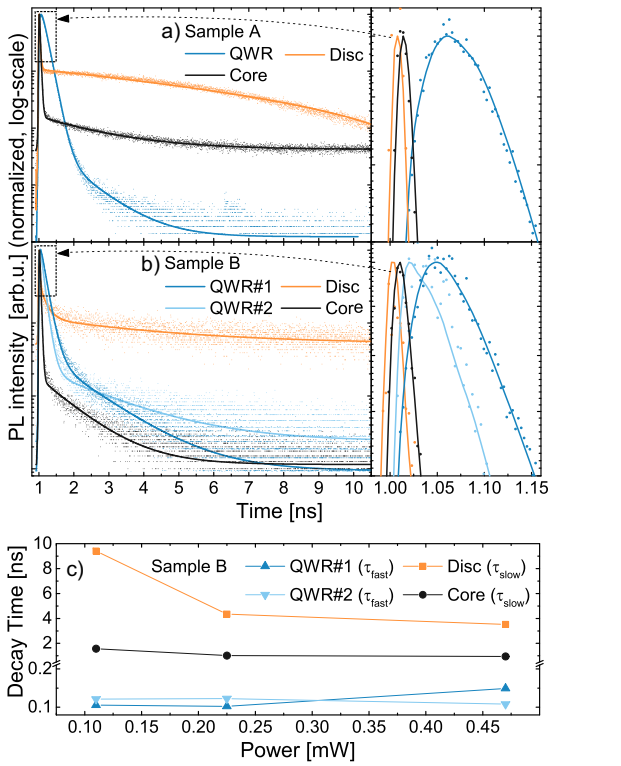

Fig. 6 (a) and (b): TR-μPL decay curves of the different emission features of the same single NWs as in Fig. 2a,b. Right hand side: Magnified time scale to illustrate the initial QWR rise time. All decays were acquired at 2000 W/cm^2 excitation power. (c) Decay times of the different emission features of sample B for different excitation power.

it was also reported in ref. 26. The existence of several peaks can be assigned to QWRs with different diameters, deposited at the edges of the same NW. However, a single QWR could also exhibit multiple emission lines, e.g. by different localization centers within one QWR, analog to studies on the emission properties of nanodiscs in NWs in ref. 38. The emission energy of the QWR band does not shift with increasing excitation power, confirming the absence of considerable internal electric fields as it was shown in Fig 3 c.

For spatial and spectral assignment of the different emission features, the question has to be addressed, how QWRs exhibit recombination rates of similar magnitude as the core and disc, despite their significantly smaller excitation volume. A possible explanation is the existence of transfer processes whose dynamic behavior can be assessed by TR-μPL as shown in Figs. 6 a and b. Decay curves for the emissions from the NW core and the disc are fitted biexponentially with a fast and slow decay component τ_{fast} and τ_{slow}. Only for the QWR emission, a triexponential fit is required due to an additional rise-time τ_{rise}, i.e. an initial fast luminescence increase before the onset of the biexponential decay. The fits employ a convolution model to account for the instrument response function (τ_{IRF}). As no structural details of sample A and B are known, the same simulations are used for the comparison with both samples ($d_{QWR} = 1.6$ nm; $d_{core} = 31.2$ nm; $h_{disc} = 15.2$ nm).

The QWR emission exhibits a fast decay component τ_{fast} (Tab. 1), which is in good agreement with the ensemble TR-PL measurements in ref. 26 (120 ps) and in the same range as the simulated QWR lifetime. For samples with a high number of QWR-related peaks we could not observe a correlation between emission energy and decay time (spectra not shown here). Assuming that different emission peaks originate from QWRs on different edges, this indicates that no transfer or feeding process between the different QWRs occurs.

However, the most striking feature is the delayed luminescence maximum of the QWR with respect to the core and disc maximum (Fig. 6 a,b, magnified plot). As for both samples the related rise time is in the same order as the fast decay time of core and disc, a carrier transfer from the latter into the QWR is the most probable explanation for this observation. In addition, comparing the two QWR peaks in sample B, the emission at lower energy shows a delayed luminescence peak, indicating, that lower energetic states are fed for a longer time.

Both, core and disc show a two-step dynamic behavior with an initially fast decay time, which is more than one order of magnitude faster than expected from the simulated optical lifetimes

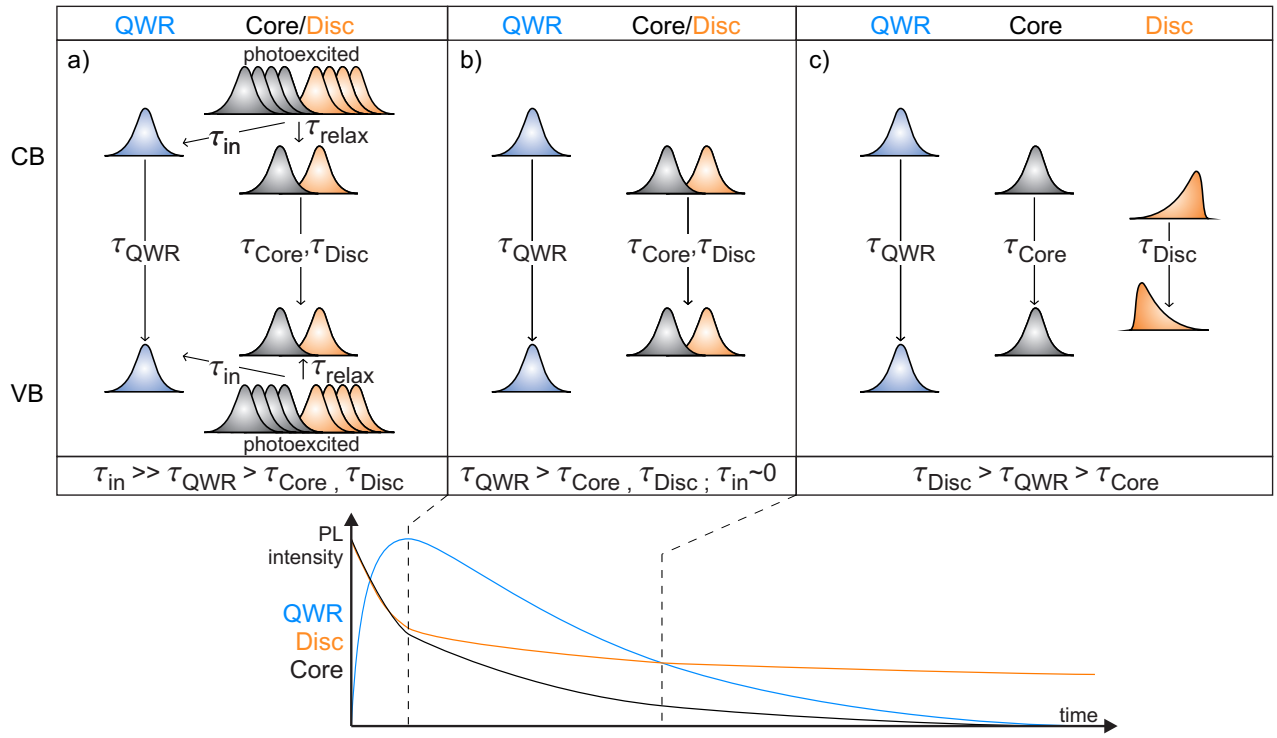

Fig. 7 Term schemes of the relative band edge state positions in the QWR, core and disc region for (a) occupied core/disc reservoir, empty QWR reservoir and screened fields; (b) occupied core/disc/QWR reservoir and screened fields; (c) occupied core/disc/QWR reservoir and increasingly unscreened fields.

and already in the range of the experimental resolution limit ($\tau_{IRF} \approx 30$ ps). This indicates that in this time interval radiative recombination is not the dominating loss term for both reservoirs. The fact, that this fast decay time is very similar to the QWR rise time, is a strong indication that the additional losses are caused by feeding of photoexcited carriers into the QWRs. The slower decay time of core and disc, which dominates the behavior in the nanosecond regime, fits reasonably well to the simulation range and can thus be assigned to radiative recombination.

The slow decay time of the disc emission (Fig. 6 a,b orange line), is in the order of several ns and in some cases even too long for the measurement timeframe of 12 ns. This can be explained by the axial band profile and the strong internal fields in the disc (Fig. 3 b). Screening of these fields by photoexcited free carriers decreases during the decay process, causing an increase of the long-living decay component and a spectral red shift.

In case of the core emission (Fig. 6 a,b black line), the luminescence decays almost completely within the measured timeframe (flat line at noise limit), when the emission is spectrally isolated (Fig. 2 b, sample B). In the case of sample A, in contrast, where the core emission shows a spectral overlap with the disc emission, the luminescence intensity remains almost constant (Fig. 2 a), which can be attributed to the long-living disc emission. The spectral overlap might also be the explanation for the discrepancy to the rather long decay time for the NBE core emission reported in ref. 26 of $\tau \approx 250$ ps (monoexponential) compared to our τ_{fast} values. In that publication TR-PL was performed on NW ensembles, hence NBE core and disc emissions could not be spectrally separated leading to mixture of their decay times.

Moreover, we have compared the decay processes for different excitation powers (Fig. 6 c) for sample B. As in the simulations, the decay time of core and QWR does not vary significantly with excitation power, respectively carrier concentration. In contrast, the disc emission systematically decays faster for higher excitation power in agreement with a reduced QCSE due to screening by photoexcited carriers.

Merging the findings of the different recombination centers we can describe the time evolution after excitation and thus the features of the transients in terms of carrier transitions and transfers using three simple term schemes (Fig. 7).

As pointed out before, the absorption of photons mainly occurs in the voluminous core and disc region. Thus, after the pulse absorption the concentration of excited electron hole pairs is significantly increased only in the core and disc as illustrated by the photoexcited carriers in Fig. 7. This drastically reduces the QCSE for the latter one leading to energetically adjacent disc and core states but empty QWR states (Fig. 7 a).

In addition to the relaxation (τ_{relax}) into the disc/core ground states, a second decay path for the photoexcited carriers exists: Feeding of the QWR reservoir due to a highly efficient transfer process reduces the carrier concentration in the disc/core region with the time-constant τ_{in}, corresponding to the fast component of the PL decay τ_{fast} extracted from the TR-PL measurements. Hence, the QWR emission increases with the same time-constant (τ_{rise}) until the QWR reservoir is filled or excited disc/core states do not longer exist.

In a subsequent step, (Fig. 7 b) the in-scattering process into the QWR is not the leading loss of the disc/core reservoir any-

more. In this phase, the global carrier concentration still screens a significant part of the intrinsic fields and thus enables the radiative recombination in all optical active regions.

With a further decay of carriers (Fig. 7 c), the disc starts to shift to lower energies and at the same time the lifetime grows by magnitudes – resulting in a non-radiative deep attractor for the remaining electron hole pairs.

0.4 Conlusion

In summary, we have shown how an innovative template-based growth approach can be used to obtain initially field free GaN QWRs with contact to relatively large carrier reservoirs.

Single NW heterostructures exhibit manifold emission features. In combination with numerical simulations, we were able to assign all optical signals within the spectral range to distinct areas of the nanostructure and presented unambiguous findings of a carrier transfer between those reservoirs. Thereby, feeding processes from the disc and the core into the QWRs were proven to be faster by one order of magnitude than optical decay.

Such processes are the fundamental pre-requisite for any future electronic or optoelectronic operation of QWR structures, as direct excitation is inefficient due to the low volume and the lateral structure geometry. Nevertheless, due to transfer processes, efficient injection of carriers into the QWR via the larger parts of the NW structure becomes possible.

0.5 Acknowledgement

We thank Marcus Müller, Alexander Reuper, Peter Veit and Jürgen Christen from the Otto-von-Guericke-Universität in Magdeburg (Germany) for useful discussions and their valuable contributions to the structure analysis with the preparation of several STEM pictures.

SMS acknowledges funding from "Programa Internacional de Becas "la Caixa"-Severo Ochoa". SMS and JA acknowledge funding from Generalitat de Catalunya 2014 SGR 1638 and the Spanish MINECO project e-TNT (MAT2014-59961-C2-2-R). ICN2 acknowledges support from the Severo Ochoa Program (MINECO, Grant SEV-2013-0295) and is funded by the CERCA Programme / Generalitat de Catalunya. Part of the present work has been performed in the framework of Universitat Autònoma de Barcelona Materials Science PhD program. Some of the research leading to these results has received funding from the European Union Seventh Framework Program under Grant Agreement 312483 - ESTEEM2 (Integrated Infrastructure Initiative - I3). Part of the HAADF-STEM microscopy was conducted in the Laboratorio de Microscopias Avanzadas at the Instituto de Nanociencia de Aragon-Universidad de Zaragoza. JA and SMS thank them for offering access to their instruments and expertise.

References

1 R. Esaki, L. and Tsu, *IBM J. Res. Dev*, 1970, **14**, 61.

2 L. Esaki and L. L. Chang, *Physical Review Letters*, 1974, **33**, 495–498.

3 L. L. Chang, L. Esaki and R. Tsu, *Applied Physics Letters*, 1974, **24**, 593–595.

4 R. Tsu and L. Esaki, *Applied Physics Letters*, 1973, **22**, 562–564.

5 R. Dingle, H. L. Störmer, A. C. Gossard and W. Wiegmann, *Applied Physics Letters*, 1978, **33**, 665–667.

6 Y. Arakawa and H. Sakaki, *Applied Physics Letters*, 1982, **40**, 939–941.

7 H. Sakaki, *Japanese Journal of Applied Physics*, 1980, **19**, L735–L738.

8 Y. Arakawa and A. Yariv, *IEEE Journal of Quantum Electronics*, 1986, **QE-22**, 1887–1899.

9 A. Yariv, *Applied Physics Letters*, 1988, **53**, 1033–1035.

10 H. Sakaki, *Journal of Vacuum Science and Technology*, 1981, **19**, 148–149.

11 A. B. Fowler, A. Hartstein and R. A. Webb, *Physical Review Letters*, 1982, **48**, 196–199.

12 W. J. Skocpol, L. D. Jackel, E. L. Hu, R. E. Howard and L. A. Fetter, *Physical Review Letters*, 1982, **49**, 951–955.

13 P. M. Petroff, A. C. Gossard, R. A. Logan and W. Wiegmann, *Applied Physics Letters*, 1982, **41**, 635–638.

14 M. Yazawa, M. Koguchi, A. Muto, M. Ozawa and K. Hiruma, *Applied Physics Letters*, 1992, **61**, 2051–2053.

15 J. Hu, T. W. Odom and C. M. Lieber, *Accounts of Chemical Research*, 1999, **32**, 435–445.

16 Y. C. Choi, W. S. Kim, Y. S. Park, S. M. Lee, D. J. Bae, Y. H. Lee, G.-S. Park, W. B. Choi, N. S. Lee and J. M. Kim, *Advanced Materials*, 2000, **12**, 746–750.

17 X. F. Duan and C. M. Lieber, *Adv. Mater.*, 2000, **12**, 298–302.

18 M. H. Huang, S. Mao, H. Feick, H. Yan, Y. Wu, H. Kind, E. Weber, R. Russo and P. Yang, *Science*, 2001, **292**, 1897–1899.

19 W. Han, S. Fan, L. Qunqing and Y. Hu, *Science*, 1997, **277**, 1287–1289.

20 B. Amstatt, J. Renard, C. Bougerol, E. Bellet-Amalric, B. Gayral and B. Daudin, *Journal of Applied Physics*, 2007, **102**, 074913.

21 W. Guo, M. Zhang, A. Banerjee and P. Bhattacharya, *Nano Letters*, 2010, **10**, 3356–3359.

22 M. Sarollahi, V. P. Kunets, Y. I. Mazur, M. Mortazavi, G. J. Salamo and M. Ware, 2017, **10099**, 100991F.

23 S. Xia, L. Liu, Y. Diao and Y. Kong, *Optical Materials*, 2017, **64**, 187–192.

24 L. T. Canham, *Applied Physics Letters*, 1990, **57**, 1046–1048.

25 X. Duan, Y. Huang, R. Agarwal, C. M. C. Lieber and C. G. Fast, *Nature*, 2003, **421**, 241–245.

26 J. Arbiol, C. Magen, P. Becker, G. Jacopin, A. A. Chernikov, S. Schäfer, F. Furtmayr, M. Tchernycheva, L. Rigutti, J. Teubert, S. Chatterjee, J. R. Morante and M. Eickhoff, *Nanoscale*, 2012, **4**, 7517–7524.

27 Y. Kato, S. Kitamura, K. Hiramatsu and N. Sawaki, *Journal of Crystal Growth*, 1994, **144**, 133–140.

28 T. Schumann, T. Gotschke, F. Limbach, T. Stoica and R. Calarco, *Nanotechnology*, 2011, **22**, 095603.

29 M. Hugues, P. A. Shields, F. Sacconi, M. Mexis, M. Auf Der Maur, M. Cooke, M. Dineen, A. Di Carlo, D. W. E. Allsopp and J. Zúniga-Pérez, *Journal of Applied Physics*, 2013, **114**,

084307.
30 O. Stier, M. Grundmann and D. Bimberg, *Physical Review B*, 1999, **59**, 5688–5701.
31 M. Winkelnkemper, A. Schliwa and D. Bimberg, *Physical Review B*, 2006, **74**, 155322/1–5.
32 M. Grundmann, O. Stier and D. Bimberg, *Physical Review B*, 1995, **52**, 11969–11981.
33 S. L. Chuang and C. S. Chang, *Physical Review B*, 1996, **54**, 2491–2504.
34 F. Furtmayr, M. Vielemeyer, M. Stutzmann, J. Arbiol, S. Estrad, F. Peir, J. R. Morante and M. Eickhoff, *Journal of Applied Physics*, 2008, **104**, 034309.
35 J. Schörmann, P. Hille, M. Schäfer, J. Müßener, P. Becker, P. J. Klar, M. Kleine-Boymann, M. Rohnke, M. De La Mata, J. Arbiol, D. M. Hofmann, J. Teubert and M. Eickhoff, *Journal of Applied Physics*, 2013, **114**, 103505.
36 D. A. B. Miller, D. S. Chemla, T. C. Damen, A. C. Gossard, W. Wiegmann, T. H. Wood and C. A. Burrus, *Physical Review Letters*, 1984, **53**, 2173–2176.
37 J. Renard, R. Songmuang, G. Tourbot, C. Bougerol, B. Daudin and B. Gayral, *Physical Review B - Condensed Matter and Materials Physics*, 2009, **80**, 121305/1–5.
38 L. Rigutti, J. Teubert, G. Jacopin, F. Fortuna, M. Tchernycheva, A. De Luna Bugallo, F. H. Julien, F. Furtmayr, M. Stutzmann and M. Eickhoff, *Physical Review B - Condensed Matter and Materials Physics*, 2010, **82**, 235308/1–7.